Direct experimental evidence of tunable charge transfer at the $LaNiO_3/CaMnO_3$ ferromagnetic interface

J. R. Paudel,[1] M. Terilli,[2] T.-C. Wu,[2] J. D. Grassi,[1] A. M. Derrico,[1] R. K. Sah,[1] M. Kareev,[2] F. Wen,[2] C. Klewe,[3] P. Shafer,[3] A. Gloskovskii,[4] C. Schlueter,[4] V. N. Strocov,[5] J. Chakhalian,[2] and A. X. Gray[1,*]

[1]*Physics Department, Temple University, Philadelphia, Pennsylvania 19122, USA*
[2]*Department of Physics and Astronomy, Rutgers University, Piscataway, New Jersey 08854, USA*
[3]*Advanced Light Source, Lawrence Berkeley National Laboratory, Berkeley, California 94720, USA*
[4]*Deutsches Elektronen-Synchrotron, DESY, 22607 Hamburg, Germany*
[5]*Swiss Light Source, Paul Scherrer Institute, 5232 Villigen, Switzerland*

(Received 13 June 2023; revised 8 August 2023; accepted 16 August 2023; published 29 August 2023)

Interfacial charge transfer in oxide heterostructures gives rise to a rich variety of electronic and magnetic phenomena. Designing heterostructures where one of the thin-film components exhibits a metal-insulator transition opens a promising avenue for controlling such phenomena both statically and dynamically. In this work, we utilize a combination of depth-resolved soft x-ray standing-wave and hard x-ray photoelectron spectroscopies in conjunction with polarization-dependent x-ray absorption spectroscopy to investigate the effects of the metal-insulator transition in $LaNiO_3$ on the electronic and magnetic states at the $LaNiO_3/CaMnO_3$ interface. We report a direct observation of the reduced effective valence state of the interfacial Mn cations in the metallic superlattice with an above-critical $LaNiO_3$ thickness (6 unit cells, u.c.) facilitated by the charge transfer of itinerant Ni $3d$ e_g electrons into the interfacial $CaMnO_3$ layer. Conversely, in an insulating superlattice with a below-critical $LaNiO_3$ thickness of 2 u.c., a homogeneous effective valence state of Mn is observed throughout the $CaMnO_3$ layers due to the blockage of charge transfer across the interface. The ability to switch and tune interfacial charge transfer enables precise control of the emergent ferromagnetic state at the $LaNiO_3/CaMnO_3$ interface and, thus, has far-reaching consequences on the future strategies for the design of next-generation spintronic devices.

DOI: 10.1103/PhysRevB.108.054441

I. INTRODUCTION

Application-driven atomic-level design of complex-oxide heterostructures that exhibit functional electronic and magnetic phenomena has become a diverse and vibrant subfield of condensed-matter physics and materials science [1–3]. Of particular interest are the materials systems wherein rich physics and intricate interplay between various degrees of freedom at the interface give rise to functional properties not observed in the constituent materials [4–8]. In such heterostructures, charge transfer across the interface often plays a key role in establishing new electronic [9–11], magnetic [12,13], and orbital [14–16] states with properties that can be tailored via dimensionality [17,18], epitaxial strain [19,20], interface termination [21,22], doping [23,24], and engineered defects [25,26]. Thus, the flexibility and diversity of the perovskite oxide structures coupled with state-of-the-art thin-film synthesis turn the fundamental and robust phenomenon of charge transfer into a powerful tuning knob for creating the desired ground state and controlling its functionality.

Epitaxial superlattices consisting of antiferromagnetic $CaMnO_3$ and paramagnetic $LaNiO_3$ exhibit emergent ferromagnetism [13] that can be tailored by varying the thickness of individual layers [27]. Such thickness dependence has been attributed to the electronic-structural changes in the $LaNiO_3$ layer, which undergoes a metal-insulator transition in the ultrathin (few unit-cell, u.c.) limit [28]. According to our current understanding based on several experimental [13,27,29,30] and theoretical studies of $LaNiO_3/CaMnO_3$ [31] and similar systems (e.g., $CaRuO_3/CaMnO_3$) [32], in metallic superlattices with an above-critical $LaNiO_3$ thickness, interfacial charge transfer mediated by the itinerant Ni $3d$ e_g electrons is expected to create an increased concentration of Mn^{3+} cations at the interface. Such charge reconstruction creates an electronic environment favorable for the emergence of the Mn^{4+}-Mn^{3+} double-exchange interaction, which stabilizes long-range canted ferromagnetic order in an approximately 1-u.c.-thick interfacial layer of $CaMnO_3$. Conversely, in superlattices with a below-critical $LaNiO_3$ thickness (<4 u.c.), partial or complete blockage of charge transfer from the now-insulating $LaNiO_3$ results in a significant (approximately threefold) suppression of the observed magnetic moment [27]. The residual magnetic moment of approximately 0.3 μ_B per interfacial Mn atom has been attributed to the presence of the Ni^{2+}-Mn^{4+} superexchange interaction made possible by the oxygen vacancies in the $LaNiO_3$ layers [27,30] that are driven to the $LaNiO_3/CaMnO_3$ interfaces by the polar mismatch. Such defects, as well as possible chemical intermixing, play a minor role and could be controlled via growth

*axgray@temple.edu

conditions and epitaxial strain [26,33]. Thus, the phenomenon of interfacial charge transfer is currently considered to be the main driving force responsible for the emergence of the long-range ferromagnetic order at the $LaNiO_3/CaMnO_3$ interface. Furthermore, the possibility of switching and tuning this magnetic phenomenon in the quantum-confined structure via either static or dynamic control of the metallicity of the $LaNiO_3$ layers makes the $LaNiO_3/CaMnO_3$ system a prime candidate for high-density spintronic devices wherein energy-efficient magnetic switching could be accomplished with electric fields or other external stimuli.

Detection and characterization of interfacial charge-transfer phenomena like the ones described above present a unique practical challenge due to the lack of direct yet non-destructive techniques capable of probing minute changes in the valence state at a buried interface with element specificity and Ångstrom-level spatial resolution. The $LaNiO_3/CaMnO_3$ heterostructure exemplifies a class of materials systems where such stringent measurement requirements are necessary due to the extremely localized nature of the phenomenon of interest.

In this paper, we report a direct observation of the tunable character of interfacial charge transfer in $LaNiO_3/CaMnO_3$ superlattices using depth-resolved soft x-ray standing-wave photoelectron spectroscopy (SW-XPS) [34]. We examined two otherwise identical superlattices containing either insulating or metallic $LaNiO_3$ layers and extracted element-specific and valence-state-sensitive spectroscopic data from the interfacial regions. Standing-wave (SW) excitations in both first-order and second-order Bragg reflection geometries were utilized to enhance the depth resolution of the technique. Our results revealed a depth-dependent modification of the effective valence state on the interfacial Mn cations in the metallic [6−u.c. $LaNiO_3$/4−u.c. $CaMnO_3$]×10 superlattice that is consistent with the enhanced charge-transfer picture. Conversely, a homogeneous effective valence state throughout the $CaMnO_3$ layers was observed for the thinner [2−u.c. $LaNiO_3$/4−u.c. $CaMnO_3$]×10 superlattice, suggesting suppression of charge transfer across the interface due to the insulating nature of the below-critical-thickness $LaNiO_3$ films. Complementary bulk-sensitive hard x-ray photoelectron spectroscopy (HAXPES) measurements of the valence-band electronic structure revealed suppression of the Ni $3d$ e_g density of states near the Fermi level, consistent with the thickness-dependent metal-insulator transition in the $LaNiO_3$ layers, which was confirmed via conventional electronic transport measurements. Concomitant suppression of the interfacial magnetic moment on the interfacial Mn sites was observed via polarization-dependent x-ray absorption spectroscopy (XAS) with x-ray magnetic circular dichroism (XMCD) at the Mn $L_{2,3}$ edges.

II. RESULTS AND DISCUSSION

A. Probing bulk-sensitive electronic and magnetic structure via HAXPES and XMCD

For our experiments, two high-quality epitaxial superlattices consisting of ten repetitions of $LaNiO_3/CaMnO_3$ were synthesized using pulsed-laser interval deposition [35] on a single-crystalline $LaAlO_3(001)$ substrate. The thickness of the $CaMnO_3$ layers in the superlattices was kept the same at 4 u.c., while the thickness of the $LaNiO_3$ layers was fixed at $N = 2$ u.c. for the first (insulating) superlattice and $N = 6$ u.c. for the second (metallic) superlattice. Thicknesses and layer-by-layer deposition were monitored *in situ* using reflection high-energy electron diffraction (RHEED). After the growth, the resultant high quality, crystallinity, and correct layering of the superlattices were confirmed *ex situ* using x-ray diffraction (XRD). Correct chemical composition was confirmed via bulk-sensitive HAXPES measurements carried out using a laboratory-based spectrometer (see Methods section in the Supplemental Material [36]). Individual thicknesses of the layers and the quality of the interfaces were confirmed using synchrotron-based SW-XPS measurements that are described in detail later in this paper (see Fig. 2). The results of the XRD, RHEED, and HAXPES characterization are presented in Figs. S1 and S2 of the Supplemental Material [36] (see also Refs. [37–40] within).

To probe the thickness-dependent variation in the valence-band electronic structure of $LaNiO_3$ and its effect on the resistivity of the superlattices, we utilized a combination of bulk-sensitive valence-band HAXPES spectroscopy at the P22 beamline [41] of the PETRA III synchrotron (DESY) (see Methods section in the Supplemental Material [36]) and electronic transport measurements. Figure 1(a) shows the experimental valence-band spectra of the $N = 6$ u.c. superlattice (red line) and the $N = 2$ u.c. superlattice (blue line). The corresponding temperature-dependent sheet-resistance curves measured using the standard van der Pauw method are shown in the inset. The near-Fermi-level region of the spectra exhibits two prominent features which, based on prior studies, correspond to the strongly hybridized Ni $3d$ e_g and t_{2g} states at 0.3 and 1.0 eV, respectively [28,42]. It is important to note that the spectral range near the Fermi level does not contain any $CaMnO_3$-derived electronic states due to its insulating nature with a band-gap "window" on the order of 1.35–3.05 eV as determined via theory and experiment, respectively [43,44]. Consistent with prior studies of the thickness-dependent metal-insulator transition in $LaNiO_3$ [28,42], the superlattice containing below-critical-thickness $LaNiO_3$ layers ($N = 2$ u.c.) exhibits a significant suppression of the near-Fermi-level electronic states resulting directly in the approximately two orders of magnitude enhancement in sheet resistivity. In the context of interfacial ferromagnetism, such bulk-sensitive HAXPES measurements demonstrate directly the depletion of the itinerant Ni $3d$ e_g states that, in metallic superlattices, facilitate charge transfer from Ni to the interfacial Mn sites, thus creating an electronic environment that stabilizes the ferromagnetic state mediated by the double-exchange interaction.

The effect of suppressing the Ni-to-Mn charge-transfer channel in the $N = 2$ u.c. superlattice is immediately evident in the element-specific (Mn) XMCD measurements of these two otherwise identical samples (see Methods section in the Supplemental Material [36]). The XAS measurements at the Mn $L_{2,3}$ edges [top panel of Fig. 1(b)] do not exhibit significant differences between the two superlattices, due to the depth-averaging nature of the technique. On the other hand, the XMCD spectra shown in the lower panels are only sensitive to the interfacial ferromagnetic state and, therefore,

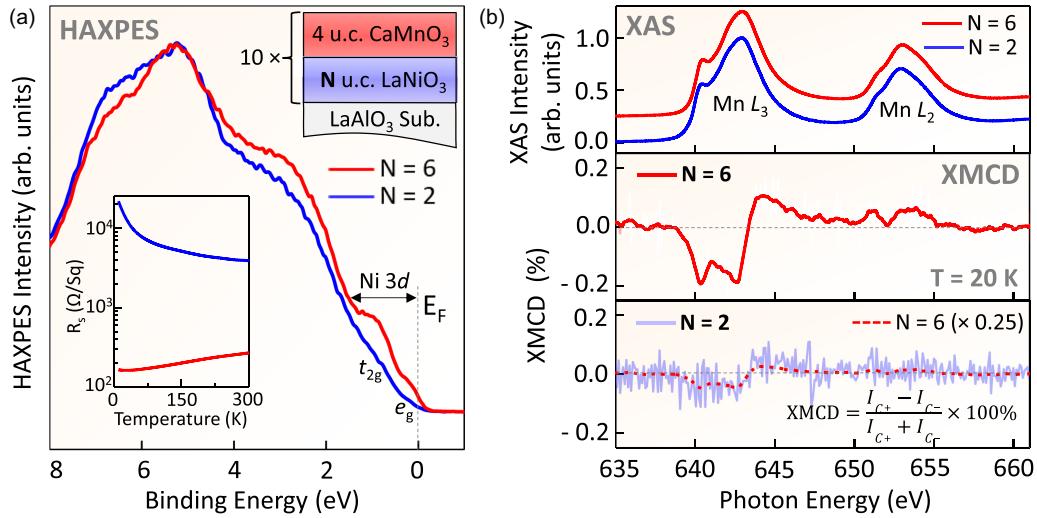

FIG. 1. (a) Angle-integrated bulk-sensitive HAXPES valence-band spectra of $N = 6$ u.c. (red line) and $N = 2$ u.c. (blue line) superlattices recorded with photon energy of 6 keV at $T = 60$ K. Significant depletion of near-E_F Ni $3d$ e_g and t_{2g} density of states results in metal-insulator transition in $N = 2$ u.c. sample, as probed with sheet-resistivity measurements shown in inset. (b) Bulk-sensitive Mn $L_{2,3}$-edge XAS spectra measured in LY detection mode at $T = 20$ K and probing entire depth of superlattice (top panel) reveal no significant differences in depth-averaged valence states of Mn between two samples. XMCD spectrum of the $N = 6$ u.c. superlattice (middle panel) shows significant magnetic signal of up to -0.20% at Mn L_3 edge. Light-red spectrum represents raw data while solid red curve has been smoothed using Savitzky-Golay method. Conversely, $N = 2$ u.c. spectrum (light-blue spectrum in bottom panel) exhibits nearly negligible XMCD signal of approximately -0.05% in same photon energy range. Solid blue spectrum represents $N = 6$ data scaled by factor of 4 ($\times 0.25$), for comparison. All XMCD measurements were carried out in applied (in-plane) magnetic field of 1.5 T.

isolate the magnetic signal from the interface (without facilitating quantitative depth resolution). Consistent with prior studies [13,27], the thicker $N = 6$ u.c. superlattice exhibits a significant XMCD signal (approximately -0.20% at the Mn L_3 edge), which is directly proportional to the magnetic moment on Mn in the interfacial region of the $CaMnO_3$ layers. Conversely, the below-critical-thickness $N = 2$ u.c. superlattice exhibits almost no discernible XMCD signal throughout the spectrum, except a slight excursion from zero (approximately -0.05%) at the photon energies corresponding to the Mn L_3 absorption threshold (640–643 eV). Such a fourfold suppression of the Mn magnetic moment is qualitatively consistent with a prior study by Flint *et al.* [27], where magnetic moments of up to 1 $\mu_{B/Mn}$ were observed for the above-critical-thickness superlattices and only 0.2 $\mu_{B/Mn}$ for the ultrathin (2-u.c. $LaNiO_3$) samples. All XMCD measurements were conducted in an applied in-plane magnetic field of 1.5 T.

B. Probing interfacial charge transfer with soft x-ray SW-XPS

Our measurements, carried out using bulk-sensitive spectroscopies such as HAXPES and XAS/XMCD (luminescence yield, LY), in concert with prior studies suggest a direct connection between the depletion of the Ni $3d$ e_g states near the Fermi level in the ultrathin ($N = 2$ u.c.) $LaNiO_3$ films and the suppression of interfacial magnetic moment on Mn sites in the adjacent $CaMnO_3$ films. In order to bridge this connection and link it to interfacial charge transfer from Ni to Mn, we have measured the depth-resolved evolution of the Mn valence state at the $LaNiO_3/CaMnO_3$ interface in both samples using soft x-ray standing-wave photoemission spectroscopy at the soft x-ray angle-resolved photoelectron spectroscopy (SX-ARPES) endstation [45] of the high-resolution ADRESS beamline at the Swiss Light Source [46]. The results are presented in Figs. 2 and 3 below.

In the SW-XPS technique, shown schematically in Fig. 2(a), Ångstrom-level depth resolution is facilitated by generating an x-ray SW interference field within a periodic superlattice sample [34,47]. The maximum-contrast modulations in the x-ray E-field intensity are achieved at the first- and second-order Bragg conditions that are typically found by varying the x-ray grazing-incidence angle at a fixed photon energy. Once the x-ray SW field is established within the sample, it can be translated vertically (perpendicular to the sample's surface) by approximately half of the superlattice period by scanning (rocking) the grazing x-ray incidence angle across the Bragg condition. In a recent soft x-ray study [48], the depth resolution of one cubic perovskite unit cell (approximately 3.8 Å) was demonstrated using the same experimental setup (see Methods section in the Supplemental Material [36]).

As the first step in such an experiment, incidence-angle-dependent "rocking curves" of the core-level intensities for several constituent elements in the superlattice are measured in the first-order Bragg condition for each sample. Typically, for unambiguous x-ray optical fitting, it is necessary to record and analyze such rocking curves for at least one element from each layer, as well as the adventitious carbon from the surface atmospheric contaminant layer [49].

Figures 2(b) and 2(c) show experimental rocking-curve spectra for the integrated intensities of the Mn $2p$, Mn $3s$, Ca $2p$, O $1s$, Ni $3p$, and C $1s$ core-level peaks measured on the $N = 6$ u.c. and $N = 2$ u.c. superlattices, respectively (circular markers). The measurements were carried out with

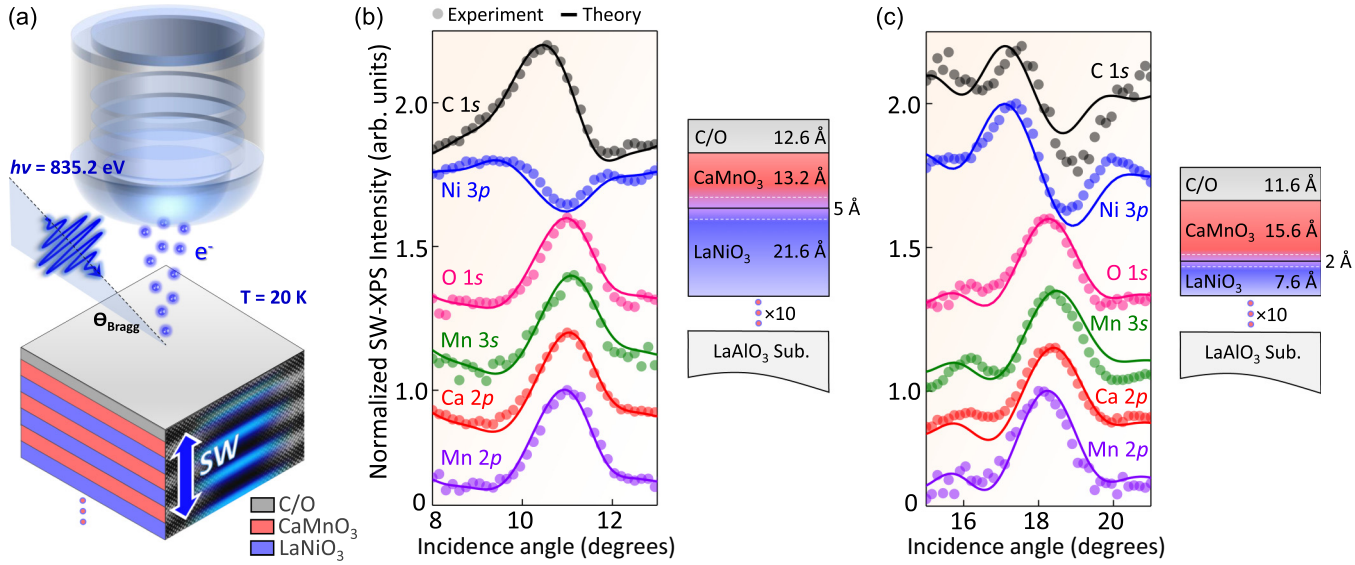

FIG. 2. (a) Schematic diagram of SW-XPS experiment and investigated superlattice structures consisting of 10 $LaNiO_3$/$CaMnO_3$ bilayers grown epitaxially on $LaAlO_3$(001) substrate, with each bilayer consisting of 4 u.c. of $CaMnO_3$ and N u.c. ($N = 6$ and 2) of $LaNiO_3$. (b) Best fits between experimental (circular markers) and calculated (solid lines) SW rocking curves for all accessible representative core levels in thicker ($N = 6$ u.c.) superlattice. Resultant depth profile yielding values of individual layer thicknesses and interface roughness (interdiffusion) is shown on right. (c) Similar results of x-ray optical fitting of experimental SW rocking curves for thinner ($N = 2$ u.c.) superlattice and resultant depth profile.

a resonant photon energy of 835.2 eV (La $3d_{5/2}$ absorption threshold) to maximize the x-ray optical contrast between $LaNiO_3$ and $CaMnO_3$ [50]. It is immediately obvious that the Mn/Ca, Ni, and C signals originate from different layers (vertical locations) within the sample due to the contrasting line shapes (phases) of their respective rocking-curve spectra. The O 1*s* rocking curve is dominated by the signal from the upper $CaMnO_3$ layer due to the limited probing depth and, therefore, resembles the Ca and Mn spectra, consistent with prior studies [30,48]. The Bragg features for the thinner ($N = 2$ u.c.) superlattice appear at higher grazing-incidence angles (16°–20°), as expected from the basic diffraction formalism.

The experimental rocking curves were simultaneously and self-consistently fitted using x-ray optical theoretical code for automatic structure optimization (see Methods section in the Supplemental Material [36]). The best fits (solid curves) to the experimental data and the resultant Ångstrom-level depth-resolved chemical profiles of the superlattices are shown in Figs. 2(b) and 2(c). The resultant total thicknesses of the 4-u.c. $CaMnO_3$ and 6-u.c. $LaNiO_3$ layers in the thicker superlattice are consistent to within 0.5 u.c with the lattice constants of 3.89 Å ($LaNiO_3$) and 3.73 Å ($CaMnO_3$) reported previously in the literature [51–53]. For the thinner ($N = 2$ u.c.) superlattice, the resultant total thicknesses are consistent within <0.2 u.c. The best-fit values of the interface roughness (interdiffusion length) are 5 Å (~1.3 u.c.) for the thicker superlattice and 2 Å (~0.5 u.c.) for the thinner superlattice, which are consistent with typical high-quality layer-by-layer growth [35]. Finally, the thickness of the surface-adsorbed contaminant layer from exposure to the atmosphere (labeled C/O) has typical values of 12–13 Å. Such an element-specific structural analysis adds to the host of other characterization results attesting to the high quality and precise control of our superlattice synthesis.

The x-ray optical models and sample structures were then used to calculate the depth-resolved profiles of the x-ray SW electric-field intensities (E^2) inside the two superlattices in the first-order Bragg condition. The purpose of such calculations is to determine the two x-ray grazing-incidence angles for each of the superlattices, wherein the antinodes (high E^2) of the standing wave preferentially highlight (1) the middle "bulklike" sections of the $CaMnO_3$ layers and (2) the interfacial sections adjacent to $LaNiO_3$. Consequently, by scanning the x-ray grazing-incidence angle between these two values, a detailed center-to-interface valence-state profile on Mn can be obtained by measuring the depth-resolved evolution of the Mn 3*s* core-level multiplet splitting [30].

The results of such calculations for the experimental geometries corresponding to the first-order Bragg condition are shown in Fig. S3 in the Supplemental Material [36]. It is evident that while the optimal experimental geometries highlighting the bulklike and interface-like sections of the $CaMnO_3$ layers can be attained for the thinner ($N = 2$ u.c.) sample [see Fig. S3(b)], the tripled thickness of the $LaNiO_3$ layers ($N = 6$ u.c.) and the nearly doubled period (10 u.c.) of the thicker superlattice preclude such depth-selective measurements with comparable contrast and depth resolution in the first-order Bragg condition [see Fig. S3(a)].

It has been suggested by Libera *et al.* [54] that carrying out x-ray SW experiments in the second-order Bragg geometry could result in an enhancement of the depth resolution due to the doubling of the SW frequency within the sample (at the expense of some diminution of the SW contrast). Thus, for the thicker superlattice ($N = 6$ u.c.) with nearly double the period (10 u.c. compared to 6 u.c.), such SW frequency doubling

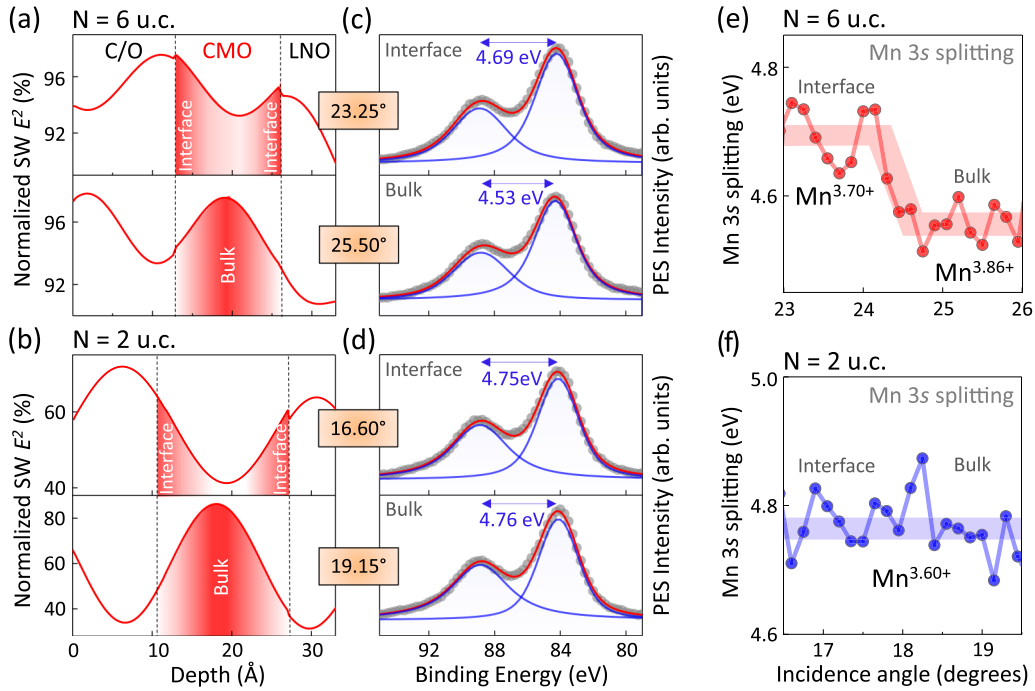

FIG. 3. (a) Simulated intensity of x-ray standing-wave electric field (E^2) inside $N = 6$ u.c. superlattice as function of depth for x-ray grazing-incidence angles of 23.25° (top panel) and 25.50° (bottom panel) sensitive to interface-like and bulklike regions of $CaMnO_3$ layer, respectively. (b) Similar simulations for $N = 2$ u.c. superlattice with characteristic x-ray incidence angles of 16.60° and 19.15° corresponding to interface-sensitive and bulk-sensitive experimental geometries, respectively. (c) Mn 3*s* core-level photoemission spectra for $N = 6$ u.c. superlattice recorded in interface-sensitive (top) and bulk-sensitive (bottom) experimental geometries, respectively. Difference in multiplet energy splitting of 0.16 eV is observed. (d) Similar measurements of Mn 3*s* core-level spectra for $N = 2$ u.c. superlattice reveal no differences in magnitude of splitting between interface and bulk. (e) Depth-dependent evolution of Mn 3*s* multiplet splitting (in eV) as function of x-ray grazing-incidence angle showing change in effective valence state of Mn in $CaMnO_3$ from +3.86 (in bulk) to +3.70 (at interface) in $N = 6$ u.c. superlattice. (f) Similar measurement for $N = 2$ u.c. superlattice, showing homogeneous Mn valence state throughout thickness of $CaMnO_3$ layers.

within the sample results in a similar SW intensity profile and, therefore, facilitates a comparable depth resolution to that seen in the thinner sample (measured in the first-order Bragg condition).

The simulated SW *E*-field intensity profiles for the optimal x-ray grazing-incidence geometries highlighting the bulklike and interface-like sections of the $CaMnO_3$ layers are shown in Fig. 3. Figure 3(a) depicts the second-order SW profiles in the topmost layers of the thicker ($N = 6$ u.c.) superlattice. It reveals that the optimal x-ray grazing incidence for probing the interface-like and bulklike sections of the $CaMnO_3$ layers are 23.25° and 25.50°, respectively. Conversely, the first-order SW profiles for the thinner ($N = 2$ u.c.) superlattice shown in Fig. 3(b) reveal the optimal angles of 16.60° (interface) and 19.15° (bulk).

To quantify the valence state of Mn in the bulk $CaMnO_3$ and at the interfaces, we carried out high-resolution measurements of the multiplet-split Mn 3*s* core-level peaks in each of the above-mentioned experimental geometries. In transition-metal oxides, the exchange-coupling interaction between the 3*s* core-hole and 3*d* electrons in the valence bands result in the splitting of the 3*s* core level [55]. The magnitude of this energy splitting is inversely proportional to the valence state of the Mn ion and, thus, can be used to estimate the said valence state [56]. To date, Mn 3*s* core-level energy-splitting XPS analysis is considered to be one of the most reliable methods for accurately quantifying changes in the Mn valence state because it does not rely on the relative peak-intensities analysis (e.g., XAS and EELS), which can be heavily affected by the background subtraction, limited energy resolution, and the degree of overlap between the peaks corresponding to different valence states (e.g., Mn $L_{2,3}$ XAS analysis).

Figures 3(c) and 3(d) show Mn 3*s* peaks for the $N = 6$ u.c. and $N = 2$ u.c. superlattices, respectively, measured and fitted self-consistently using two Voigt line shapes after a Shirley background subtraction. The two panels in each figure correspond to the interface-like and bulklike experimental geometries characterized by the x-ray grazing-incidence angle and the SW *E*-field intensity profile shown on the left of the plot.

It is clear that even with the lower SW contrast for the second-order Bragg geometry, a significant increase in the magnitude of the Mn 3*s* energy splitting (∼160 meV) for the $N = 6$ u.c. superlattice is observed at the interface ($\Delta E = 4.69$ eV) as compared to bulklike $CaMnO_3$ ($\Delta E = 4.53$ eV). These values of splitting can be used to estimate the formal valence state of the Mn cation in the bulk and at the interface of the 4-u.c.-thick $CaMnO_3$ film [56], which yields values of +3.86 (near-stoichiometric +4) for the bulk and +3.70 (reduced by 0.16 e^-) at the interface.

It is important to note that the observed bulk-to-interface change in the Mn 3*s* multiplet splitting (∼160 meV) is approximately 70% larger than our total experimental energy resolution (95 meV). However, since the two multiplet components of the Mn 3*s* peaks are well separated by nearly 5 eV, our ability to quantify the central positions of the corresponding Voigt peaks is much better than 95 meV and is more closely related to the energy stability of the beamline (<10 meV).

In contrast to this, for the thinner ($N = 2$ u.c.) superlattice, the magnitudes of the Mn 3*s* core-level multiplet splitting are virtually identical at 4.75 eV (interface) and 4.76 eV (bulk). This result suggests that the valence state of Mn cations in the thinner ($N = 2$ u.c.) superlattice does not evolve with depth or as a function of proximity to the interface with $LaNiO_3$. Due to a higher SW contrast in the first-order Bragg geometry, our measurement for the thinner superlattice is even more sensitive to depth-dependent changes. It is important to reiterate here that the only difference between the two superlattices investigated in this study is the thickness (and thus metallicity) of the $LaNiO_3$ layers. The thickness of the $CaMnO_3$ layers (4 u.c.) as well as the number of layers in the superlattice (10) are the same for both samples.

To further confirm our findings and to investigate the depth-dependent evolution of the Mn valence state in both samples, we scanned the x-ray grazing-incidence angle in 0.2° steps between the two "extreme" SW conditions, effectively translating the SW antinode from the interface to the central section of the 4-u.c.-thick $CaMnO_3$ film. The resultant plots of the Mn 3*s* core-level multiplet splittings (in eV) as a function of the x-ray grazing-incidence angle are shown in Figs. 3(e) and 3(f) using the same relative vertical (energy) scales.

For the thicker ($N = 6$ u.c.) superlattice [Fig. 3(e)], a clear steplike decrease in the magnitude of the splitting is observed over the range of x-ray grazing-incidence angles spanning the second-order Bragg condition (24°–25°). In this narrow angular range, the intensity contrast of the SW within the sample is maximized, and its phase changes (shifts) from interface sensitive to bulk sensitive. These findings suggest that the formal valency of the Mn cations changes from approximately +3.86 to +3.70 over a distance of 2 u.c. from bulk to interface, respectively. Thus, the interfacial unit cells of $CaMnO_3$ in the superlattice with thicker (metallic) $LaNiO_3$ layers host an increased concentration of Mn^{3+} cations compared to bulk. The electronic (charge-transfer) nature of this phenomenon is strongly evidenced by the absence of such interfacial valency reduction in the superlattice with the below-critical-thickness (insulating) $LaNiO_3$ layers, as shown in Fig. 3(f).

It is important to note that some minor but measurable oscillation in the magnitude of the Mn 3*s* splitting is observed at both lower (interface-sensitive) and higher (bulk-sensitive) x-ray grazing-incidence angles. Such oscillations are typically observed in SW-XPS measurements of core-level intensities as well as x-ray reflectivity and are termed the Kiessig (or Fresnel) fringes [50]. The intensity modulations result in modulations of the SW contrast (or amplitude). Thus, at certain x-ray grazing-incidence angles (e.g., 23.7°), we observe some averaging between the interface-like and bulklike Mn 3*s* energy-splitting values.

Previous studies have suggested that the reduced effective valence state of the interfacial Mn cations in metallic superlattices with an above-critical $LaNiO_3$ thickness occurs due to charge transfer of itinerant Ni 3*d* e_g electrons to Mn in the interfacial $CaMnO_3$ layer [13,27,30]. The resultant charge reconstruction at the interface creates an electronic environment favorable for the emergence of the Mn^{4+}-Mn^{3+} double-exchange interaction, which stabilizes a long-range canted ferromagnetic order. Conversely, in the insulating superlattices with below-critical $LaNiO_3$ thickness, the depletion of the Ni 3*d* e_g states at the Fermi level results in a partial or complete blockage of charge transfer from Ni to Mn and thus prevents the stabilization of the ferromagnetic state. Prior to this study, the amount of charge transfer necessary to stabilize the ferromagnetic order in $CaMnO_3$ was calculated to be in the wide range of 0.07–0.20 e^- per Mn cation [32].

Thus, our current results establish a direct connection between the depletion of Ni 3*d* e_g states (measured via HAXPES) that results in the metal-insulator transition in $LaNiO_3$ (measured via electronic transport) and the suppression of the charge-transfer-induced ferromagnetic state in $CaMnO_3$ (measured via Mn $L_{2,3}$ XMCD). Furthermore, we directly observe the depth-dependent reduction of the Mn valency by 0.16 e^- at the interface with metallic $LaNiO_3$ [Fig. 3(e)]—an amount that is consistent with the prior theoretical prediction of the charge transfer to Mn in a similar materials system (0.07–0.20 e^-) [32]. In contrast to this, in a similar superlattice with insulating $LaNiO_3$, no such change in the interfacial Mn valency is observed [Fig. 3(f)], consistent with the charge-transfer suppression scenario. The above-mentioned quantitative agreement between our work and theory further supports the explanation that the magnetism is tuned by the charge transfer across the interface, rather than by the emergence of defects and/or additional interfacial phases (e.g., $La_{1-x}Ca_xMnO_3$). Density-functional theory and spin-sensitive experimental techniques, such as resonant inelastic x-ray scattering and neutron scattering, are critical to shed light on the detailed interfacial spin structures in this material system.

It is important to note that neither of the two samples contains perfectly stoichiometric $CaMnO_3$ with an effective Mn valence state of 4+. This is typically the case with coherently epitaxial $CaMnO_3$ films under tensile strain due to the formation of oxygen vacancies [26]. The SW-XPS measurements of the thinner ($N = 2.$ u.c.) superlattice [see Fig. 3(f)] yield a lower average valence state of Mn (+3.60) due to several experimental factors, such as a higher surface sensitivity of the first-order SW measurement as well as a possibly slightly higher tensile strain at the surface of the thinner superlattice (less relaxation) leading to more oxygen vacancies. Our bulk-sensitive HAXPES measurements of the Mn 3*s* core-level splitting confirm the same depth-averaged Mn valence state (+3.85) in both superlattices (see Figure S4(a) in the Supplemental Material [36]), which is consistent with the similarly bulk-sensitive XAS (LY) measurements shown in Fig. 1(b). To confirm the surfacelike origin of the lower valence state of Mn in the thinner ($N = 2$ u.c.) sample, we carried out additional surface-sensitive Mn $L_{2,3}$ XAS measurements using the total electron-yield detection mode,

which facilitates an average probing depth of only ~ 5 nm [57]. The results are shown in Fig. S4(d) of the Supplemental Material [36] and reveal a significant increase in the intensities of the Mn^{3+} features at the lower photon-energy side of the Mn L_3 absorption edge (at ~ 639–641 eV), thus confirming the surface origin of this effect. An extended discussion is provided in the Supplemental Material [36].

It is also important to note that the strain state of $CaMnO_3$ has been shown to have no measurable effect on interfacial ferromagnetism in prior studies [53]. In fact, a significant interfacial ferromagnetic moment on Mn was observed even for the samples grown in a different crystallographic orientation (111 as opposed to 001) [58]. Thus, any minor structural differences between the two measured samples are not likely to have a significant effect on the electronic and magnetic structure at the interface.

III. SUMMARY AND CONCLUSIONS

In conclusion, we used a combination of bulk-sensitive valence-band HAXPES, magnetic spectroscopy, and electronic transport measurements to probe layer-resolved electronic and magnetic properties of $LaNiO_3/CaMnO_3$ superlattices. Our results established a direct connection between the depletion of the Ni $3d$ e_g states leading to the metal-insulator transition in $LaNiO_3$ and the concomitant suppression of the interfacial ferromagnetic state in $CaMnO_3$. We then utilized depth-resolved SW-XPS in both first- and second-order Bragg reflection geometries to link the emergence of interfacial ferromagnetism in $CaMnO_3$ to the direct observation of Ni-Mn charge-transfer induced valence-state change (by $0.16\,e^-$) of the interfacial Mn cations in the metallic ($N = 6$ u.c.) superlattice. The tunable (or switchable) character of this phenomenon was demonstrated by tailoring the thickness of the individual $LaNiO_3$ layers in the high-quality layer-by-layer grown $LaNiO_3/CaMnO_3$ superlattices. Our results provide a recipe for designing next-generation spintronic devices using charge-transfer phenomena for efficient tuning and switching of low-dimensional electronic and magnetic states at interfaces.

ACKNOWLEDGMENTS

J.R.P., J.D.G., A.M.D., R.K.S., and A.X.G. acknowledge support from the U.S. Department of Energy, Office of Science, Office of Basic Energy Sciences, Materials Sciences and Engineering Division under Award No. DE-SC0019297. The electrostatic photoelectron analyzer for the lab-based HAXPES measurements at Temple University was acquired through an Army Research Office DURIP Grant No. W911NF-18–1–0251. A.X.G. also gratefully acknowledges the support from the Alexander von Humboldt Foundation. M.T., T.-C.W., M.K., and J.C. acknowledge support from the Department of Energy under Grant No. DE-SC0012375. C.K. and P.S acknowledge support from the U.S. Department of Energy, Office of Science, Office of Basic Energy Sciences, the Microelectronics Co-Design Research Program, under Contract No. DE-AC02-05-CH11231 (Codesign of Ultra-Low-Voltage Beyond CMOS Microelectronics). This research used resources of the Advanced Light Source, which is a DOE Office of Science User Facility under Contract No. DE-AC02-05CH11231. We acknowledge DESY (Hamburg, Germany), a member of the Helmholtz Association HGF, for the provision of experimental facilities. Beamtime at DESY was allocated for Proposal No. I-20210142. Funding for the HAXPES instrument at beamline P22 by the Federal Ministry of Education and Research (BMBF) under framework program ErUM is gratefully acknowledged.

[1] J. A. Sulpizio, S. Ilani, P. Irvin, and J. Levy, Annu. Rev. Mater. Res. **44**, 117 (2014).
[2] A. Bhattacharya and S. J. May, Annu. Rev. Mater. Res. **44**, 65 (2014).
[3] X. Liu, S. Middey, Y. Cao, M. Kareev, and J. Chakhalian, MRS Commun. **6**, 133 (2016).
[4] P. Zubko, S. Gariglio, M. Gabay, P. Ghosez, and J.-M. Triscone, Annu. Rev. Condens. Matter Phys. **2**, 141 (2011).
[5] D. Xiao, D. Zhu, Y. Ran, N. Nagaosa, and S. Okamoto, Nat. Commun. **2**, 596 (2011).
[6] H. Y. Hwang, Y. Iwasa, M. Kawasaki, B. Keimer, N. Nagaosa, and Y. Tokura, Nat. Mater. **11**, 103 (2012).
[7] J. Chakhalian, J. W. Freeland, A. J. Millis, C. Panagopoulos, and J. M. Rondinelli, Rev. Mod. Phys. **86**, 1189 (2014).
[8] H. Chen and A. J. Millis, J. Phys.: Condens. Matter **29**, 243001 (2017).
[9] H. Chen, A. J. Millis, and C. A. Marianetti, Phys. Rev. Lett. **111**, 116403 (2013).
[10] Y. Cao, X. Liu, M. Kareev, D. Choudhury, S. Middey, D. Meyers, J. W. Kim, P. Ryan, J. W. Freeland, and J. Chakhalian, Nat. Commun. **7**, 10418 (2016).
[11] C. Schlueter, C. Aruta, N. Yang, A. Tebano, D. Di Castro, G. Balestrino, and T. L. Lee, Phys. Rev. Mater. **3**, 094406 (2019).
[12] K. S. Takahashi, M. Kawasaki, and Y. Tokura, Appl. Phys. Lett. **79**, 1324 (2001).
[13] A. J. Grutter, H. Yang, B. J. Kirby, M. R. Fitzsimmons, J. A. Aguiar, N. D. Browning, C. A. Jenkins, E. Arenholz, V. V. Mehta, U. S. Alaan, and Y. Suzuki, Phys. Rev. Lett. **111**, 087202 (2013).
[14] J. Chakhalian, J. W. Freeland, H.-U. Habermeier, G. Cristiani, G. Khaliullin, M. van Veenendaal, and B. Keimer, Science **318**, 1114 (2007).
[15] J. Chaloupka and G. Khaliullin, Phys. Rev. Lett. **100**, 016404 (2008).
[16] P. Hansmann, X. Yang, A. Toschi, G. Khaliullin, O. K. Andersen, and K. Held, Phys. Rev. Lett. **103**, 016401 (2009).
[17] S. Middey, D. Meyers, D. Doennig, M. Kareev, X. Liu, Y. Cao, Z. Yang, J. Shi, L. Gu, P. J. Ryan, R. Pentcheva, J. W. Freeland, and J. Chakhalian, Phys. Rev. Lett. **116**, 056801 (2016).
[18] A. Arab, X. Liu, O. Köksal, W. Yang, R. U. Chandrasena, S. Middey, M. Kareev, S. Kumar, M.-A. Husanu, Z. Yang, L. Gu,

V. N. Strocov, T.-L. Lee, J. Minár, R. Pentcheva, J. Chakhalian, and A. X. Gray, Nano Lett. **19**, 8311 (2019).

[19] Y. Chen, F. Trier, T. Kasama, D. V. Christensen, N. Bovet, Z. I. Balogh, H. Li, K. T. S. Thydén, W. Zhang, S. Yazdi, P. Norby, N. Pryds, and S. Linderoth, Nano Lett. **15**, 1849 (2015).

[20] F. Motti, G. Vinai, A. Petrov, B. A. Davidson, B. Gobaut, A. Filippetti, G. Rossi, G. Panaccione, and P. Torelli, Phys. Rev. B **97**, 094423 (2018).

[21] A. Rubano, T. Günter, T. Fink, D. Paparo, L. Marrucci, C. Cancellieri, S. Gariglio, J.-M. Triscone, and M. Fiebig, Phys. Rev. B **88**, 035405 (2013).

[22] A. Malashevich, M. S. J. Marshall, C. Visani, A. S. Disa, H. Xu, F. J. Walker, C. H. Ahn, and S. Ismail-Beigi, Nano Lett. **18**, 573 (2018).

[23] C. Schlueter, N. Yang, C. Mazzoli, C. Cantoni, A. Tebano, D. Di Castro, G. Balestrino, P. Orgiani, A. Galdi, J. Herrero-Martín, P. Gargiani, M. Valvidares, and C. Aruta, Adv. Quantum Technol. **3**, 2000016 (2020).

[24] J. Gabel, M. Zapf, P. Scheiderer, P. Schütz, L. Dudy, M. Stübinger, C. Schlueter, T.-L. Lee, M. Sing, and R. Claessen, Phys. Rev. B **95**, 195109 (2017).

[25] M. Huijben, G. Koster, M. K. Kruize, S. Wenderich, J. Verbeeck, S. Bals, E. Slooten, B. Shi, H. J. A. Molegraaf, J. E. Kleibeuker, S. van Aert, J. B. Goedkoop, A. Brinkman, D. H. A. Blank, M. S. Golden, G. van Tendeloo, H. Hilgenkamp, and G. Rijnders, Adv. Funct. Mater. **23**, 5240 (2013).

[26] R. U. Chandrasena, W. Yang, Q. Lei, M. U. Delgado-Jaime, K. D. Wijesekara, M. Golalikhani, B. A. Davidson, E. Arenholz, K. Kobayashi, M. Kobata, F. M. F. de Groot, U. Aschauer, N. A. Spaldin, X. X. Xi, and A. X. Gray, Nano Lett. **17**, 794 (2017).

[27] C. L. Flint, H. Jang, J.-S. Lee, A. T. N'Diaye, P. Shafer, E. Arenholz, and Y. Suzuki, Phys. Rev. Mater. **1**, 024404 (2017).

[28] P. D. C. King, H. I. Wei, Y. F. Nie, M. Uchida, C. Adamo, S. Zhu, X. He, I. Božović, D. G. Schlom, and K. M. Shen, Nat. Nanotechnol. **9**, 443 (2014).

[29] C. L. Flint, A. Vailionis, H. Zhou, H. Jang, J.-S. Lee, and Y. Suzuki, Phys. Rev. B **96**, 144438 (2017).

[30] R. U. Chandrasena, C. L. Flint, W. Yang, A. Arab, S. Nemšák, M. Gehlmann, V. B. Özdöl, F. Bisti, K. D. Wijesekara, J. Meyer-Ilse, E. Gullikson, E. Arenholz, J. Ciston, C. M. Schneider, V. N. Strocov, Y. Suzuki, and A. X. Gray, Phys. Rev. B **98**, 155103 (2018).

[31] J. Jilili, I. Tolbatov, F. Cossu, A. Rahaman, B. Fiser, and M. Upadhyay Kahaly, Sci. Rep. **13**, 5056 (2023).

[32] B. R. K. Nanda, S. Satpathy, and M. S. Springborg, Phys. Rev. Lett. **98**, 216804 (2007).

[33] M. Golalikhani, Q. Lei, R. U. Chandrasena, L. Kasaei, H. Park, J. Bai, P. Orgiani, J. Ciston, G. Sterbinsky, D. A. Arena, P. Shafer, E. Arenholz, B. Davidson, A. J. Millis, A. X. Gray, and X. X. Xi, Nat. Commun. **9**, 2206 (2018).

[34] C.-T. Kuo, G. Conti, J. E. Rault, C. M. Schneider, S. Nemšàk, and A. X. Gray, J. Vac. Sci. Technol. A **40**, 020801 (2022).

[35] M. Kareev, S. Prosandeev, B. Gray, J. Liu, P. Ryan, A. Kareev, E. J. Moon, and J. Chakhalian, Appl. Phys. Lett. **109**, 114303 (2011).

[36] See Supplemental Material at http://link.aps.org/supplemental/10.1103/PhysRevB.108.054441 for detailed experimental and simulation methods, x-ray diffraction and RHEED characterization, chemical characterization using HAXPES, x-ray standing-wave E-field intensity simulations, and surface and bulk-sensitive Mn valence-state analysis using HAXPES and XAS. The Supplemental Material also contains Refs. [37–40].

[37] A. Jablonski and C. J. Powell, J. Vac. Sci. Technol. A **27**, 253 (2009).

[38] A. T. Young, E. Arenholz, J. Feng, H. Padmore, S. Marks, R. Schlueter, E. Hoyer, N. Kelez, and C. Steier, Surf. Rev. Lett. **9**, 549 (2002).

[39] U. Aschauer, R. Pfenninger, S. M. Selbach, T. Grande, and N. A. Spaldin, Phys. Rev. B **88**, 054111 (2013).

[40] A. F. Zurhelle, D. V. Christensen, S. Menzel, and F. Gunkel, Phys. Rev. Mater. **4**, 104604 (2020).

[41] C. Schlueter, A. Gloskovskii, K. Ederer, I. Schostak, S. Piec, I. Sarkar, Yu. Matveyev, P. Lömker, M. Sing, R. Claessen, C. Wiemann, C. M. Schneider, K. Medjanik, G. Schönhense, P. Amann, A. Nilsson, and W. Drube, AIP Conf. Proc. **2054**, 040010 (2019).

[42] A. X. Gray, A. Janotti, J. Son, J. M. LeBeau, S. Ueda, Y. Yamashita, K. Kobayashi, A. M. Kaiser, R. Sutarto, H. Wadati, G. A. Sawatzky, C. G. Van de Walle, S. Stemmer, and C. S. Fadley, Phys. Rev. B **84**, 075104 (2011).

[43] U. Aschauer and N. A. Spaldin, Appl. Phys. Lett. **109**, 031901 (2016).

[44] J. H. Jung, K. H. Kim, D. J. Eom, T. W. Noh, E. J. Choi, J. J. Yu, Y. S. Kwon, and Y. Chung, Phys. Rev. B **55**, 15489 (1997).

[45] V. N. Strocov, X. Wang, M. Shi, M. Kobayashi, J. Krempasky, C. Hess, T. Schmitt, and L. Patthey, J. Synchrotron Rad. **21**, 32 (2014).

[46] V. N. Strocov, T. Schmitt, U. Flechsig, T. Schmidt, A. Imhof, Q. Chen, J. Raabe, R. Betemps, D. Zimoch, J. Krempasky, X. Wang, M. Grioni, A. Piazzalunga, and L. Patthey, J. Synchrotron Rad. **17**, 631 (2010).

[47] S.-H. Yang, B. S. Mun, A. W. Kay, S.-K. Kim, J. B. Kortright, J. H. Underwood, Z. Hussain, and C. S. Fadley, Surf. Sci. Lett. **461**, L557 (2000).

[48] W. Yang, R. U. Chandrasena, M. Gu, R. M. S. dos Reis, E. J. Moon, A. Arab, M.-A. Husanu, S. Nemšák, E. M. Gullikson, J. Ciston, V. N. Strocov, J. M. Rondinelli, S. J. May, and A. X. Gray, Phys. Rev. B **100**, 125119 (2019).

[49] S. Nemšák, G. Conti, A. X. Gray, G. Pálsson, C. Conlon, D. Eiteneer, A. Keqi, A. Rattanachatta, A. Y. Saw, A. Bostwick, L. Morescini, E. Rotenberg, V. N. Strocov, M. Kobayashi, T. Schmitt, W. Stolte, S. Ueda, K. Kobayashi, A. Gloskovskii, W. Drube *et al.*, Phys. Rev. B **93**, 245103 (2016).

[50] A. X. Gray, C. Papp, B. Balke, S.-H. Yang, M. Huijben, E. Rotenberg, A. Bostwick, S. Ueda, Y. Yamashita, K. Kobayashi, E. M. Gullikson, J. B. Kortright, F. M. F. de Groot, G. Rijnders, D. H. A. Blank, R. Ramesh, and C. S. Fadley, Phys. Rev. B **82**, 205116 (2010).

[51] J. Chakhalian, J. M. Rondinelli, J. Liu, B. A. Gray, M. Kareev, E. J. Moon, N. Prasai, J. L. Cohn, M. Varela, I. C. Tung, M. J. Bedzyk, S. G. Altendorf, F. Strigari, B. Dabrowski, L. H. Tjeng, P. J. Ryan, and J. W. Freeland, Phys. Rev. Lett. **107**, 116805 (2011).

[52] M. C. Weber, M. Guennou, N. Dix, D. Pesquera, F. Sánchez, G. Herranz, J. Fontcuberta, L. López-Conesa, S. Estradé, F. Peiró, J. Iñiguez, and J. Kreisel, Phys. Rev. B **94**, 014118 (2016).

[53] C. L. Flint, A. J. Grutter, C. A. Jenkins, E. Arenholz, and Y. Suzuki, J. Appl. Phys. **115**, 17D712 (2014).

[54] J. A. Libera, R. W. Gurney, S. T. Nguyen, J. T. Hupp, C. Liu, R. Conley, and M. J. Bedzyk, Langmuir **20**, 8022 (2004).

[55] C. S. Fadley and D. A. Shirley, Phys. Rev. A **2**, 1109 (1970).
[56] V. R. Galakhov, M. Demeter, S. Bartkowski, M. Neumann, N. A. Ovechkina, E. Z. Kurmaev, N. I. Lobachevskaya, Y. M. Mukovskii, J. Mitchell, and D. L. Ederer, Phys. Rev. B **65**, 113102 (2002).
[57] F. M. F. De Groot, J. Electron Spectrosc. Relat. Phenom. **67**, 529 (1994).
[58] C. L. Flint, D. Yi, E. Karapetrova, A. T. N'Diaye, P. Shafer, E. Arenholz, and Y. Suzuki, Phys. Rev. Mater. **3**, 064401 (2019).